Ultrasonics 56 (2015) 417–426

Contents lists available at ScienceDirect

Ultrasonics

journal homepage: www.elsevier.com/locate/ultras

Diffraction, attenuation, and source corrections for nonlinear Rayleigh wave ultrasonic measurements

David Torello [a,*], Sebastian Thiele [b], Kathryn H. Matlack [a], Jin-Yeon Kim [b], Jianmin Qu [c], Laurence J. Jacobs [a,b]

[a] GW Woodruff School of Mechanical Engineering, Georgia Institute of Technology, Atlanta, GA 30332, United States
[b] School of Civil and Environmental Engineering, Georgia Institute of Technology, Atlanta, GA 30332, United States
[c] Department of Civil and Environmental Engineering, Northwestern University, Evanston, IL 60208, United States

ARTICLE INFO

Article history:
Received 12 May 2014
Received in revised form 12 September 2014
Accepted 14 September 2014
Available online 22 September 2014

Keywords:
Diffraction effects
Attenuation effects
Source nonlinearity
Nonlinear Rayleigh waves
Nonlinear acoustics

ABSTRACT

This research considers the effects of diffraction, attenuation, and the nonlinearity of generating sources on measurements of nonlinear ultrasonic Rayleigh wave propagation. A new theoretical framework for correcting measurements made with air-coupled and contact piezoelectric receivers for the aforementioned effects is provided based on analytical models and experimental considerations. A method for extracting the nonlinearity parameter β_{11} is proposed based on a nonlinear least squares curve-fitting algorithm that is tailored for Rayleigh wave measurements. Quantitative experiments are conducted to confirm the predictions for the nonlinearity of the piezoelectric source and to demonstrate the effectiveness of the curve-fitting procedure. These experiments are conducted on aluminum 2024 and 7075 specimens and a $\beta_{11}^{7075}/\beta_{11}^{2024}$ measure of 1.363 agrees well with previous literature and earlier work. The proposed work is also applied to a set of 2205 duplex stainless steel specimens that underwent various degrees of heat-treatment over 24 h, and the results improve upon conclusions drawn from previous analysis.

1. Introduction

Nonlinear ultrasonic measurements using Rayleigh surface waves have been successfully employed to characterize material damage and microstructural changes due to a variety of failure and plastic deformation mechanisms, including fatigue [1,2], cold work [3], thermal aging [4], and creep [5]. These methods capitalize on the generation of a second harmonic component of amplitude A_2 resulting from the interrogation of a material with a monochromatic source at a fundamental frequency of amplitude A_1. These finite amplitude Rayleigh wave components are measured at multiple locations along the central axis of the ultrasonic beam, providing amplitude information as a function of propagation distance. In previous works, it's been shown that the normalized second harmonic amplitude (A_2/A_1^2) exhibits an increasing trend with propagation distance. For short ranges of propagation, the normalized second harmonic amplitude is fit well by a linear relationship, and the slope of this function is proportional to the acoustic nonlinearity parameter β of the material. It has been shown that nonlinear effects related to coupling conditions [2] or system nonlinearity [6] do not have an experimentally significant impact on the measurement of β when measured over short distances because these effects exist equally at all measurement intervals. For this reason, this technique is attractive for field application due to its simplicity and robustness.

The exploitation of nonlinear stress–strain relationships to generate auxiliary signal components from monochromatic inputs has numerous applications in addition to the second harmonic generation (SHG) methods detailed in this work, including wave mixing phenomena [7,8] and parametric arrays [9,10]. The primary distinction between SHG and the latter two examples is that SHG focuses entirely on relating the harmonics generated from a monochromatic input to the nonlinearity of the material, whereas wave mixing and parametric array excitation seeks to exploit the material nonlinearity to produce output waves at sum and/or difference frequencies from multiple monochromatic inputs. Despite some advantages (super-directivity of outputs and temporal isolation from inputs), the latter techniques are experimentally challenging for Rayleigh wave-based applications [11].

Since the source transducer used to generate the Rayleigh wave is finite sized and directive, the radiated ultrasonic beam experiences diffraction. This manifests as oscillatory behavior in the near field, decreasing fundamental amplitude versus propagation distance, and a nonlinearly increasing and subsequent decreasing in the second harmonic amplitude in the far field. While previous literature indicates a linear increase in second harmonic amplitude, this is not generally correct and exists primarily because the propagation distance is

* Corresponding author.
E-mail address: david.torello@gmail.com (D. Torello).

http://dx.doi.org/10.1016/j.ultras.2014.09.008
0041-624X/

too small in these studies to see the combined effects of diffraction and attenuation dominating second harmonic generation. This paper attempts to rectify the calculation of the nonlinearity parameter in Rayleigh wave experiments with more accurate accounting of the effects of diffraction, attenuation, and source nonlinearities.

The diffraction of a low amplitude ultrasonic beam is well understood for both three-dimensional and two-dimensional cases [12–14], and accurate corrections for diffraction effects have been applied to the measured apparent ultrasonic wave speed and attenuation coefficient [12]. The diffraction of the second harmonic wave is somewhat more complicated than that of the fundamental since the spreading and interference of individual rays from the source are supplemented by the spatial generation of the second harmonic waves as the fundamental propagates through the nonlinear material. In the case of longitudinal wave nonlinear ultrasonic experiments, the diffraction of the nonlinear signal can generally be neglected because the propagation distance is both fixed in distance and small compared to the transducer width, which leads to minimal spreading. In addition, an integral solution has been provided for longitudinal second harmonic propagation from a piston source [15], making this correction less difficult.

However, in Rayleigh wave nonlinear ultrasonic measurements, it is crucial to take the diffraction effects into account because the measurements are done as a function of propagation distance and tend to extend into the far field, leading to an experimentally significant reduction in amplitude. Despite the fact that bulk measurements undergo more severe energy loss from these effects (on the order of $1/r^2$ for bulk waves versus $1/r$ for Rayleigh waves), the large propagation distances and the fact that the measurement relies on changes in wave amplitudes versus distance means that ignoring diffraction effects will lead to significantly different values of calculated β the further the total measurement distance is extended. For Rayleigh or Lamb waves, the derivation of a general expression for the diffraction of the second harmonic wave is intractable, however Shull et al. [16] investigated analytically and numerically the diffraction effects in nonlinear Rayleigh waves by employing the parabolic approximation in the spectral Hamiltonian formalism [17], leading to a set of partial differential equations for the fundamental and second harmonic components. Hurley [18] compared measurements taken with a laser interferometer and a generating comb transducer, characterized as a uniform finite-area source, to the theoretical results based on Shull et al. and obtained a strong match between experiment and model.

In this work, we examine the source conditions of a wedge method Rayleigh wave generation scheme with finite area circular transducers in order to determine the spatial distribution of the source amplitude as well as its harmonic content. We then apply this to a mathematical formulation based on the models proposed by Shull et al. and calculate the nonlinearity parameter β with the use of a nonlinear least squares curve-fitting algorithm in a process optimized to facilitate convergence and accuracy of the calculations in this context. This process corrects for the diffraction, attenuation, and source nonlinearity terms to ensure accurate measures of β from experimental data. Verification of this method is then provided by applying it to experimental results obtained from Al 2024 and Al 7075 sample measurements and also to a set of 2205 duplex stainless steel specimens that have undergone various durations of thermal aging.

2. Background and theory

2.1. Wave propagation derivations

The following section will provide a basic overview of the derivation of the useful equations used in this research to correct for the diffraction, attenuation, and source nonlinearity of a Rayleigh wave nonlinearity measurement setup. A more detailed accounting of the derivation is provided in Appendix A. If we consider a Rayleigh wave propagating along a surface in the x-direction of a semi-infinite half space as shown in Fig. 1(a), then we can describe the in-plane (x-axis) and out-of-plane (z-axis) particle velocities at $z = 0$ with the following equations [16,17]:

$$v_x(x,y,0,t) = (\xi_t + \eta)\sum_{n=-\infty}^{\infty} v_n(x,y)e^{in(k_0x-\omega_0t)} \tag{1}$$

$$v_z(x,y,0,t) = (1 + \xi_l\eta)\sum_{n=-\infty}^{\infty} v_n(x,y)e^{in(k_0x-\omega_0t)} \tag{2}$$

where the index n denotes the harmonic number, $\xi_t = (1-\xi^2)^{1/2}$, $\xi_l = (1-\xi^2(c_t^2)/(c_l^2))^{1/2}$, $\eta = -2(1-\xi^2)^{1/2}/(2-\xi^2)$, $\xi = c_R/c_t, c_l$ is the longitudinal phase velocity, c_t is the shear phase velocity, and c_R is the Rayleigh phase velocity.

Shull et al. showed that, utilizing a quasilinear assumption, the equations of motion for the fundamental and second harmonics of the system are [16]:

$$\left(\frac{\partial}{\partial x} + \frac{1}{2ik_0}\frac{\partial^2}{\partial y^2} + \alpha_1\right)v_1 = 0 \tag{3}$$

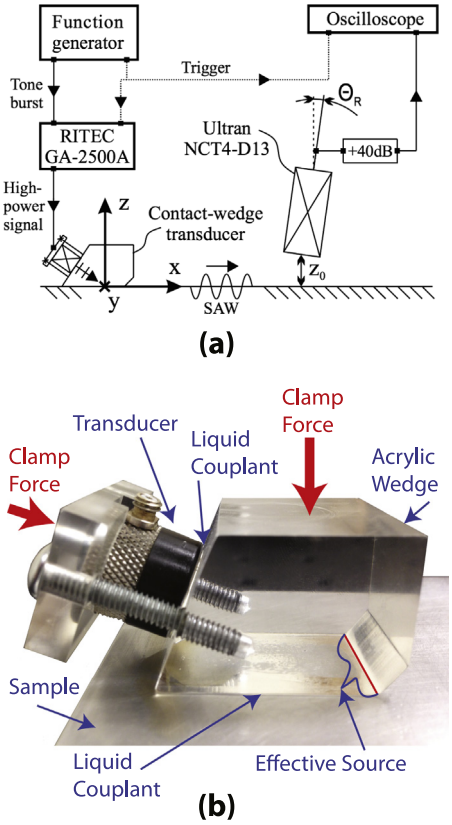

Fig. 1. (a) Experimental setup schematic and theoretical framework for air-coupled transducer measurements and wedge-method generation of Rayleigh waves on the sample surface. Propagation direction of the Rayleigh wave indicated by the above arrow is positive x direction, and the transverse direction along the face of the wedge is the y-direction, where $y = 0$ corresponds to the center of the wedge/transducer. $z = 0$ refers to the surface of the sample and becomes negative with surface depth. (b) Photograph of a contact transducer/wedge pair, noting location of the transducer, clamping forces, coupling interfaces, and the location of the effective line source (denoted by the red line). (For interpretation of the references to colour in this figure legend, the reader is referred to the web version of this article.)

$$\left(\frac{\partial}{\partial x}+\frac{1}{4ik_0}\frac{\partial^2}{\partial y^2}+\alpha_2\right)v_2=\frac{\beta_{11}k_0}{2c_R}v_1^2 \tag{4}$$

where the subscripts 1 and 2 denote the fundamental and second harmonic components respectively and α_n denotes the attenuation coefficient at these frequencies.

In the above equations we see the nonlinearity parameter β_{11}, which is ultimately what we will be attempting to characterize in the later parts of this work. β_{11} is defined by the relationship

$$\beta_{11}=\frac{4\mu R_{11}}{\zeta\rho c_R^2} \tag{5}$$

where μ is the shear modulus, ρ is the material density, $\zeta=\xi_t+\xi_t^{-1}+\eta^2(\xi_l+\xi_l^{-1})+4\eta$, and R_{11} is calculated based on the third order elastic constants (TEOCs) of the material and is defined by Shull et al. elsewhere [19]. The nonlinearity parameter is theoretically calculable with knowledge of the material TEOCs, but these parameters are notoriously hard to measure empirically [20] and the parameter β_{11} is therefore typically calculated by fitting data points with the appropriate mathematical model. In this work, the models used for curve-fitting are the solutions to Eqs. (3) and (4) using the physical parameters of the experimental setup.

If we assume that the generating transducer combined with the acrylic wedge shown in Fig. 1(b) creates a Gaussian line source, the solutions to Eqs. (3) and (4) simplify greatly. If the source function has the Gaussian form

$$f(y,t)=v_{0,1}e^{-(y/a_1)^2}e^{-i\omega t} \tag{6}$$

where $v_{0,1}$ is the peak source amplitude at ω, and a_1 is the source width, then the solution for the fundamental and second harmonic components of the wave can be solved for using integral solutions and the appropriate Green's functions, arriving at the solutions for v_1 and v_2:

$$v_1(x,y)=\frac{v_{0,1}e^{-\alpha_1 x}}{\sqrt{1+ix/x_0}}\exp\left(\frac{-(y/a_1)^2}{1+ix/x_0}\right) \tag{7}$$

$$\begin{aligned}v_2(x,y)=&\frac{i\sqrt{\pi}\beta_{11}v_{0,1}^2k_0^2a_1^2}{4c_R\sqrt{i(\alpha_2-2\alpha_1)(x_0+ix)}}\\&\times\exp\left(-\alpha_2 x-\frac{2(y/a_1)^2}{1+ix/x_0}+i(\alpha_2-2\alpha_1)x_0\right)\\&\times\left\{\operatorname{erf}\left[\sqrt{i(\alpha_2-2\alpha_1)(x_0+ix)}\right]-\operatorname{erf}\left[\sqrt{i(\alpha_2-2\alpha_1)x_0}\right]\right\}\end{aligned} \tag{8}$$

where $x_0=k_0a_1^2/2$ is the Rayleigh distance and signifies the transition from near field to far field effects.

The magnitude of the fundamental particle velocity is a function of propagation distance, x, and is dependent on the peak source amplitude and the source width ($v_{0,1}$ an a_1 respectively), as well as α_1 (a material parameter). The magnitude of the second harmonic velocity is more complicated and additionally depends on the material parameters β_{11} and α_2. The traditional definition of the nonlinear parameter, $\beta'\propto A_2/A_1^2$, is much more mathematically complicated when calculated using the solutions in Eqs. (7) and (8) than in cases where attenuation and diffraction effects are ignored [1], and the physical intuition provided by the initial definition of β' in these earlier works is obscured. It therefore makes more sense to fit the data to Eqs. (7) and (8) and extract the nonlinearity parameter from the best fitting solution.

Plotting the functions for v_1 and v_2 in the x–y plane and assuming an attenuation relationship of $\alpha_n=n^4\alpha_1$, the result shown in Fig. 2 generally describes the velocity profiles of the first two frequency components resulting from Rayleigh wave excitation. These plots are generated from Eq. (7) for the fundamental velocity profile and Eq. (8) for the second harmonic velocity profile. The fundamental particle velocity decreases monotonically from the Gaussian boundary condition at $x=0$. Additionally, the second harmonic wave increases in magnitude along the central axis and then, at a large enough distance, diffraction and attenuation effects gradually overcome the effects of harmonic generation and the magnitude begins to decrease.

At $x=0$, the predicted amplitude of the second harmonic excitation is zero, according to Fig. 2 and Eq. (8). This is because the monochromatic source term defined in Eq. (6) naturally forces this condition to be true. In reality, piezoelectric sources generally exhibit noticeable nonlinear behavior and the nonlinearity generated by the source itself, v_2^{T} (the superscript T denotes transducer), must be factored into the physical considerations of this problem for the calculation of β_{11} to be accurate. A revised source term including an initial second harmonic excitation is now considered as an input to the system of Eqs. (3) and (4)

$$f(y,t)=v_{0,1}e^{-(y/a_1)^2}e^{-i\omega t}+v_{0,2}e^{-(y/a_2)^2}e^{-2i\omega t} \tag{9}$$

where $v_{0,2}$ is the peak source amplitude for the second harmonic component of the source output and a_2 is the half width of the second harmonic component.

By using this formulation of the sourcing function $f(y,t)$, the solution for the fundamental wave remains unchanged, and the solution for the second harmonic wave now can be separated into two components as follows

$$v_2^{\mathrm{TOT}}=v_2^{\mathrm{M}}+v_2^{\mathrm{T}} \tag{10}$$

where v_2^{M} corresponds to the second harmonic wave generated in the material as the fundamental wave propagates along x as described in Eq. (8), and v_2^{T} corresponds to the nonlinearity of the source, which takes the same form as a fundamental wave propagating through the material at frequency 2ω and with properties corresponding to the material and source at this frequency. Together, the sum of these terms is equal to the total v_2, signified as v_2^{TOT}. Mathematically, the second harmonic wave due to the source nonlinearity is expressed in the following form:

$$v_2^{\mathrm{T}}(x,y)=\frac{v_{0,2}e^{-\alpha_2 x}}{\sqrt{1+ix/2x_0}}\exp\left(-\frac{(y/a_2)^2}{1+ix/2x_0}\right) \tag{11}$$

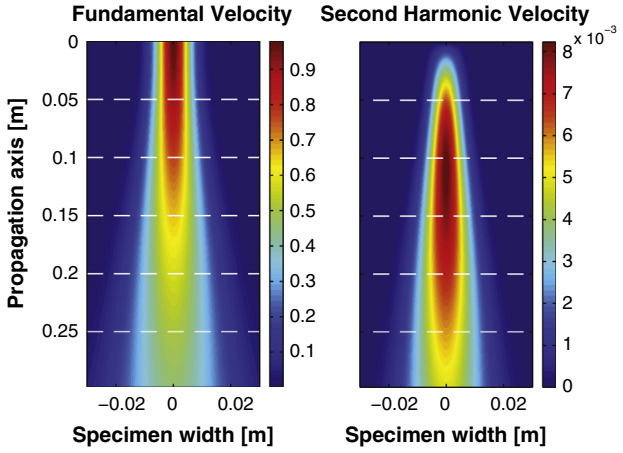

Fig. 2. x–y Plots of the particle velocity distributions for Rayleigh waves excitation from a Gaussian line source from Eqs. (7) and (8) on the left and right respectively. In these plots, the propagation axis refers to x-direction and the specimen width refers to the y-direction from Eqs. (7) and (8). The fundamental velocity decays monotonically from the Gaussian boundary condition at $x=0$, while the second harmonic velocity magnitude begins at zero and increases in magnitude from generation effects before reaching a maximum and decreasing due to attenuation and diffraction effects.

Eq. (11) differs from Eq. (7) in many ways. The attenuation of Eq. (7), α_1, is replaced in Eq. (11) by α_2 because the source nonlinearity occurs at 2ω. Similarly, the x_0 terms in Eq. (7) are replaced with $2x_0$ for the same reason. The final difference is the replacement of a_1 with a_2, which follows from the fact that the source has different apparent half-widths at every frequency.

The result of decomposing the measured second harmonic signal into the framework of Eq. (10) is shown graphically in Fig. 3 for values along the propagation axis at $y = 0$, after converting the Rayleigh particle velocities v_2^{TOT}, v_2^{M}, and v_2^{T} into displacement amplitudes A_2^{TOT}, A_2^{M}, and A_2^{T} respectively. Note that because the Rayleigh particle velocities and the corresponding displacement amplitudes are directly related, they are referred to interchangeably in the context of this work.

2.2. Curve-fitting theory

The fitting process employed in the calculation of β_{11} is a nonlinear least squares curve-fitting procedure that optimizes according to the algorithm

$$\min_x \| v_n(\{v_{0,n}, \alpha_n, \beta_{11}\}, x) - v_n^{\mathrm{MEAS}} \|_2^2 = \min_x \sum_i \left[v_n(\{v_{0,n}, \alpha_n, \beta_{11}\}, x_i) - v_{n,i}^{\mathrm{MEAS}} \right]^2 \quad (12)$$

where v_n represents the velocity functions being optimized, which in the case of the current work are v_1 in Eq. (7) for the fundamental frequency data ($n = 1$) and v_2^{TOT} in (10) for the second harmonic data ($n = 2$). Similarly, v_n^{MEAS} represents the measured velocities at their respective frequencies. The arguments to v_n include the values of the fitting parameters $\{v_{0,n}, \alpha_n, \beta_{11}\}$ and the propagation distance x. Note that β_{11} is not a relevant parameter for $n = 1$. The subscript i appearing on the right hand side of Eq. (12) indicates discrete data, in this case relating to the data obtained experimentally, which implies that minimizing the cost function in terms of the experimental data solves the overall optimization problem. This method of calculating β_{11} has been examined under different conditions and with different optimization parameters in earlier works [18].

Many of the pieces of information required for calculation of this fit are difficult to observe and quantify with the current iteration of the experimental setup and available equipment. These parameters become curve-fitting parameters themselves in order to guarantee that they are correctly accounted for in the fitting process, however adding additional parameters can increase the likelihood of a false fit due to the introduction of local minima in the optimization space. Because blind fitting to these parameters amplifies the risk of solutions at local minima, the optimizer is seeded with guesses for the input parameters that are based on theoretical and experimental insight. The effect is twofold: the optimizer converges to a solution closest to values that make physical sense, and the optimization time is reduced. The correct starting guesses for the optimization parameters are either obtained from theory, comparable literature values, or experiments. The complete data-processing and curve-fitting procedures used in the experiments performed in this paper are detailed in Fig. 4, but germane to this discussion are the steps in Fig. 4(c) and (d). In Fig. 4(c), the fundamental amplitude is used to find values of $v_{0,1}$ and α_1, which is a well-defined optimization because the amplitude is almost entirely defined by $v_{0,1}$ and the shape of the data is defined by α_1. These values are used later in the fitting process for the second harmonic data, which is first fit using a linear approximation over the first n data points depending on the qualitative size of the "linear region" to get an initial value for $v_{0,2}$ in (d). By providing physically grounded and internally consistent values for these optimization steps, the final fitting in step (e), where the second harmonic information is fit using Eq. (10), can be assured to conform to the physics of the problem.

The process until the step shown in Fig. 4(c) is nearly identical to the results published on this topic by Thiele [6] on measurements taken with air-coupled transducer setups. However, that work measures the parameter $\beta' \propto A_2/A_1^2$ instead of calculating β_{11} as described in Shull et al. [19].

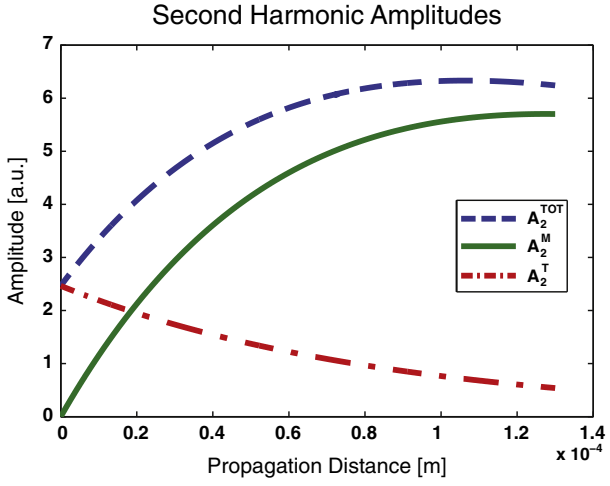

Fig. 3. Values of A_2^{TOT}, A_2^{T}, and A_2^{M} predicted by theory derived in Eqs. (8) and (9). Note that the material nonlinearity starts at zero while the actual recorded amplitude of the signal does not, which is accounted for by the peak value of transducer nonlinearity.

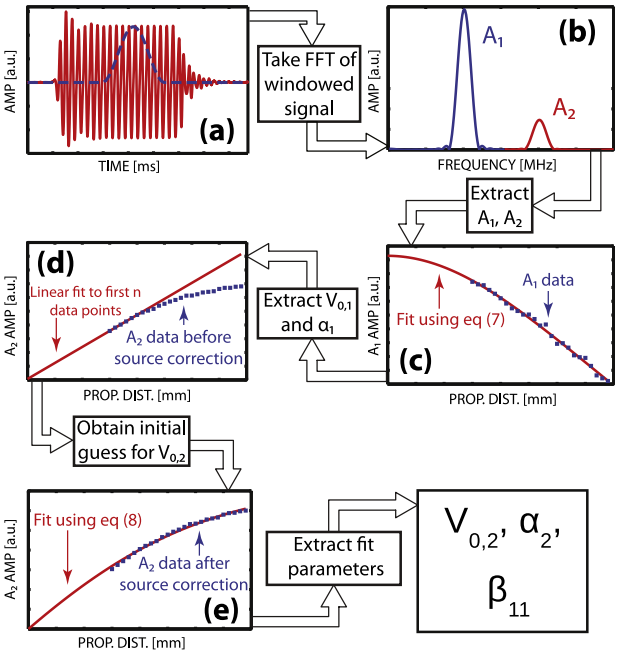

Fig. 4. Diagrammatic representation of the curve-fitting procedure used to calculate the nonlinearity parameter of the measured specimen. (a) Shows the signal from the receiving transducer (red) and the Hann window (dashed blue) used to filter it. This is processed with an FFT and (b) shows the frequency content at the fundamental (blue) and the second harmonic (red). The fundamental amplitude is then fit using Eq. (7) in (c), and the fit parameters $v_{0,1}$ and α_1 are extracted and used later to fit the second harmonic data. The second harmonic data without source correction is linearly fit using the first n data points (between 5 and 10) in order to get an initial value of $v_{0,2}$ to which the curve-fitting process is sensitive. This is then used in (e) to fit the A_2 data while correcting for the source nonlinearity. The resulting values of the fitting parameters are the desired results. (For interpretation of the references to colour in this figure legend, the reader is referred to the web version of this article.)

The step shown in Fig. 4(c) provides the basic source strength and attenuation information from the fundamental frequency component of the filtered response, but it's important to remember that these values are affected by the transfer functions of all of the components in the system (two transducers, electrical equipment, etc.). Therefore these parameters are all relative until these transfer functions are identified.

Fig. 4(d) is important because it provides an initial guess for the curve-fitting parameters in the step shown in part (e) and is essential for ensuring convergence and solution accuracy. The result of the nonlinear curve-fitting operation in Fig. 4(e) is the final value of the nonlinear source strength, the second harmonic attenuation, and ultimately β_{11}.

3. Experimental setup and procedure

3.1. Source profile measurements

3.1.1. Experimental setup

The ultrasonic generating transducer and the wedge shown in Fig. 1(b) combine to create an effective line source at the boundary where the wedge and the sample meet. To measure the shape and magnitude of this effect, a Polytec single-point laser vibrometer was used, consisting of an OFV-551 fiber optic sensor head, an OFV-5000 controller, and a custom-built x–y scanning system mounted vertically. The sample under test was a piece of 2024 aluminum. The generating setup is shown schematically in Fig. 5, using a half-inch Panametrics V-type transducer with a nominal center frequency of 2.25 MHz to generate longitudinal waves in an acrylic wedge, exciting the Rayleigh waves on the specimen surface. The applied signal was generated by an Agilent 33250A signal generator and amplified by a RITEC GA-2500A RF Amplifier, which was used because of its exceptional linearity characteristics and clean output.

The signal coming directly from the laser vibrometer was amplified through a Panametrics 5072PR pulser/receiver, providing an amplification factor of 20 dB. Furthermore, the signal was discretized using a combination of a Cleverscope CS328A and a Tektronix TDS 5034B digital oscilloscope and later analyzed in MATLAB.

3.1.2. Experimental procedure

The transducer was first applied to the wedge and clamped into position using light lubrication oil as an acoustic couplant, and this assembly was further clamped to the specimen and coupled acoustically with the same oil. Then, an input signal of 2.1 MHz over 20 cycles with a pulse repetition rate of 20 ms was applied to the generating transducer, which then propagated through the acrylic wedge to the surface.

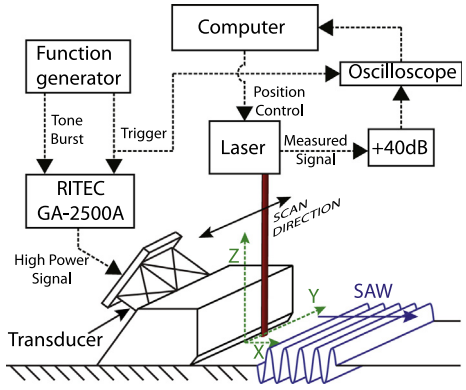

Fig. 5. Laser measurement schematic showing the measurement of the effective line source at the interface between the wedge and the sample.

The resulting Rayleigh wave was measured by aligning the laser vibrometer to the front surface of the wedge such that it was as close to the contact point between the wedge and the surface as possible. The laser was scanned in the y-direction (along the face of the wedge), and the Cleverscope and digital oscilloscope recorded the signal, averaging over 512 cycles and sampling with a rate of 250 MS/s. The data was saved using a Labview script and imported into MATLAB for data processing.

3.1.3. Data processing

To obtain the fundamental and second harmonic frequency components of the signal, the averaged and amplified time domain data was filtered using a Hann window in the steady state portion of the received signal. This effectively eliminated the ringing of the generating transducer. The signal was then processed using the MATLAB FFT algorithm and the contributions of the fundamental and second harmonics to the signal were extracted and assessed. Finally, the fundamental frequency data was fit to the corresponding frequency term in the Gaussian objective function represented by equation (9), and likewise for the second harmonic data and the corresponding term at 2ω. This was performed in the optimization toolbox in MATLAB.

3.2. Air-coupled transducer measurements

3.2.1. Experimental setup and procedure

The air-coupled transducer measurements were obtained with the setup depicted in Fig. 1. Thiele et al. covers the measurement procedure in detail in a previous work on this subject[6]. A basic summary of the measurement follows here.

The generating system is again an acrylic wedge coupled with an ultrasonic generating transducer (Panametrics V-type, center frequency of 2.25 MHz and 12.5 mm diameter), excited by an Agilent 33250A signal generator amplified by a RITEC GA-2500A RF Amplifier. The input pulse shape was again a 2.1 MHz sine wave modulated by a rectangular window of 20 cycles with a pulse repetition rate of 20 ms. The receiver is an Ultran NCT4-D13 12.5 mm diameter air-coupled transducer, amplified by a factor of 40 dB by the pulser/receiver and held at a distance of 3.5 mm from the surface of the specimen under test.

Propagation distances for this experiment were chosen between $x_{min} = 30$ mm and $x_{max} = 78$ mm, with the starting distance chosen primarily because of restrictions from the size of the air-coupled transducer and the assembly that houses it. Two millimeter step sizes provided adequate spatial resolution to see the major observable effects while maintaining a reasonable measurement time. The measurements were conducted first by calibrating the lateral position and angle and of the main lobe at the fundamental frequency and then the scans were performed by manually adjusting the x–y position of the air-coupled transducer to maintain this line. This is very important for repeatability of the results [21].

The air-coupled transducer was scanned along this centerline at a constant standoff height of 3.5 mm from the surface at an angle of approximately 6.5° for the aluminum sample. The physical method that the air-coupled transducer uses for detection of the out-of-plane displacement of the Rayleigh wave is the leakage of energy from the surface of the specimen into the air according to the predictions and theory developed by Deighton et al. [22] and is a consequence of Snell's Law, which predicts the transducer must be angled at Θ_R, where

$$\Theta_R = \sin^{-1}\left(\frac{c_{air}}{c_R}\right) \tag{13}$$

This out of plane displacement was then related back to the definition of the Rayleigh particle displacement by the relationship established by Eq. (2).

The air-coupled transducer has a nominal center frequency of 4 MHz and an actual center frequency of 3.9 MHz. The second harmonic in this measurement system (at 4.2 MHz) falls within the bandwidth of the transducer. Amplification and averaging over 256 cycles resulted in an SNR of 54 dB for these measurements, which is enough to resolve the second harmonic data adequately. This data was recorded on the Tektronix oscilloscope and imported into MATLAB for data processing.

3.2.2. Data processing

The data processing conducted on the measurements follows the process diagram shown in Fig. 4. First the data is Hann windowed and processed with an FFT algorithm to provide the amplitudes of the harmonic components. Following this process, the fundamental frequency amplitude over propagation distance is fit to Eq. (7) using the nonlinear least squares method described in Eq. (12). From this we obtained values for $\nu_{0,1}$ and α_1, which propagate throughout the procedure.

When the second harmonic data is examined, there tends to be a "linear" region, where the data looks to more or less follow a linearly increasing trend. This region extends for an arbitrary number of data points depending on the material and measurement conditions and is difficult to consistently and accurately define. However, the current method relies on only a first order approximation of the source strength, which in this case is the y-intercept of the second harmonic amplitude data, and for this purpose, the first 5–10 data points served to provide the initial fitting condition for $\nu_{0,2}$.

Finally, the data is fit to Eq. (10) with the fitting variables $\nu_{0,2}$, α_2, and β_{11}. The initial guess value for α_2 is $16\alpha_1$ based on thermoviscous attenuation predictions of the form $\alpha_n = n^4\alpha_1$ [23,18], however the final value tends to change dramatically from the guessed value and is one of the most sensitive parameters in the fitting process. From this final curve-fit, the value of β_{11} is calculated and extracted.

The data fitting described here is done using a model that assumes that all the data is being taken on the axis $y = 0$, while in reality the air-coupled transducer receives pressure wave signals from an area distribution on the material surface. The transducer face will serve as a weighting function based on its response to pressure inputs, and this complicated relationship would be important to remember for the purposes of absolute measurements. However, the measures in this work are relative, so this effect is temporarily ignored for ease of calculation and the use of axial solutions to the fitting equations is sufficient for these purposes.

4. Results and discussion

4.1. Source nonlinearity measurements

The results of the source nonlinearity measurements described in Section 3.1.1 show that there are indeed higher harmonic components to the signal that propagates from the contact interface between the acrylic wedge and the sample specimen, and that these are the only frequency components contained in the source signal. Looking at the distribution along the y-axis at the fundamental and second harmonic frequencies ($x = 0$) gives the results shown in Fig. 6.

Fig. 6 suggests that the fundamental (a) and second harmonic (b) data is fit accurately by a Gaussian profile, with R-squared values of .904 and .703 respectively. The R-squared value can be interpreted as the proportion of the variation in the data that is accounted for by the model in question, so a perfect model will give a value of 1. In this case, the fit of the fundamental source term is very high, with only roughly a ten percent variation in the data not being accounted for by a Gaussian fit, and there is high qualitative agreement. The second harmonic performs slightly worse with a value of .703, but the reduction of the R-squared value can come from many sources not related to the goodness of fit. Some of these conditions present in this system are basic variances in the data acquisition at low signal amplitudes approaching the noise floor of the receiver (the second harmonic amplitudes are very small) as well as surface conditions and slight misalignment of the optics, which would affect the SNR of the measurement system. Thus a high qualitative agreement, mixed with a reasonably high R-squared value, is confirmation that a Gaussian model accurately fits the second harmonic data.

Another observable effect is that the Gaussian beam width produced at the second harmonic is smaller than that produced at the fundamental. The fundamental beam width was measured to have a half-width, which corresponds to the radial term a in the Gaussian source equation, of 6.53 mm. This is slightly larger than the radius of the transducer, and is evidence that there is diffraction and perhaps second harmonic effects occurring within the wedge during generation. The second harmonic beam half-width was 2.69 mm, which makes sense according to standard acoustic considerations [24] and the graphical results observed from Fig. 2. Aside from confirming physical assumptions about the data,

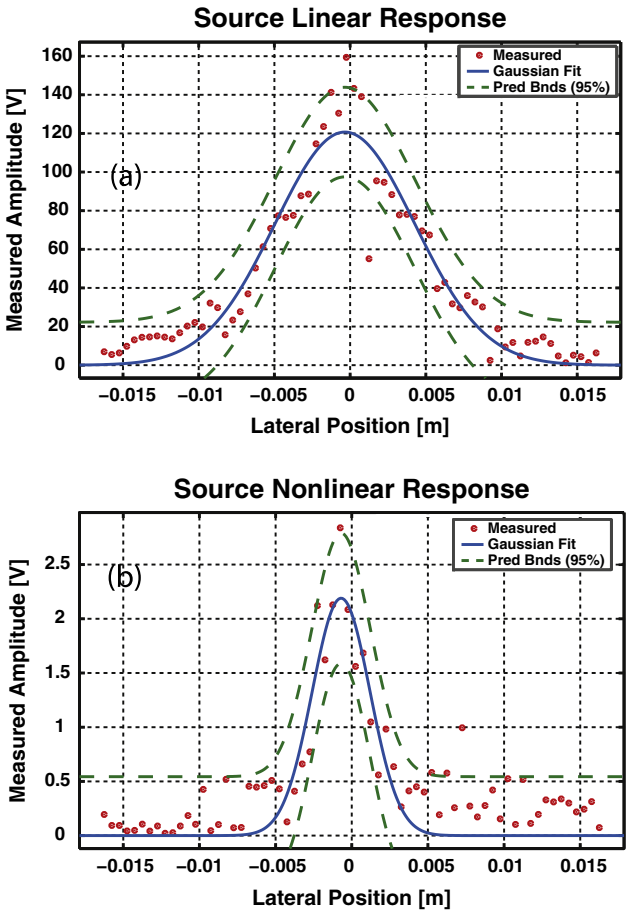

Fig. 6. The response at $x = 0$ from the transducer at the fundamental (a) and second harmonic (b) frequencies versus the distance from center of the wedge in the y-direction. Also included are the prediction bounds for a 95% confidence interval surrounding the curve fit, which is a Gaussian in profile.

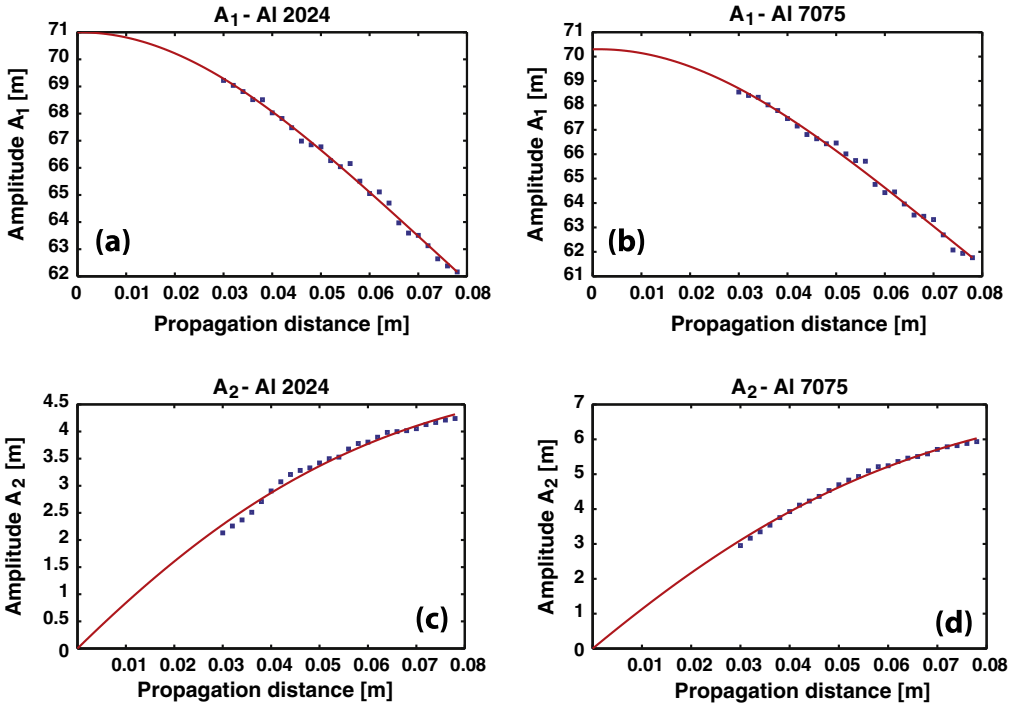

Fig. 7. Nonlinear ultrasound testing results for the Al 2024 and 7075 samples. (a) and (b) Show the fundamental amplitudes for the 2024 and 7075 specimens respectively. (c) and (d) Show the second harmonic amplitudes for the 2024 and 7075 specimens respectively. Data points and best-fit lines from the optimization process outlined in Fig. 4 are shown for each case.

this information is important for numerical considerations and determining the values of parameters in the quasilinear solutions.

For the proposed theoretical framework for analyzing β_{11} with nonlinear Rayleigh waves to be valid, the source must be a line source with Gaussian amplitude profile at all frequencies of interest [16]. The preceding analysis has demonstrated all of these conditions to be true, and thus the solutions determined in Eqs. (7) and (8) are applicable to the experiments performed in this work, as well as any nonlinear Rayleigh wave experiment that satisfies these source conditions.

4.2. Nonlinear ultrasound measurements

The results of the aluminum 2024-T351 and 7075-T651 plate measurements [25] are shown in Fig. 7. In these figures, the fundamental components (a and b) and the second harmonic components (c and d) of the received signals in Al 2024 and 7075 respectively are shown along with the results of the curve-fitting process. When interpreting these figures, it is again important to understand that fitting the values of parameters that exclusively affect the amplitude of the data will produce numerical results that are relative to transfer functions of the measurement equipment. Therefore, without precise calibration of these transfer functions, the numerical results must either be normalized or compared across specimens making sure that the source strength $\upsilon_{0,1}$ is comparable in value (which should be the case for consistent measurements regardless). In this case, the curve-fit value of $\upsilon_{0,1}$ was 9.368e8 [a.u.] for Al 2024 and 9.267e8 [a.u.] for Al 7075, which is a 1.08% difference between the two. This means that the relative amplitudes between the two methods can be compared with confidence.

The shapes of the figures are defined by their generation and decay rates, and are thus dependent on the terms inside the exponential, radical, and error functions of Eqs. (7) and (8). The relationships between the effects these terms have on the shape of the data versus scaling effects are quite complicated, which makes them very sensitive to change during the curve-fitting process. While the source strength values tend to converge very quickly, the terms that affect the shape of the data change dramatically and have a stronger influence on the quality of the fit. That being said, one of the great strengths of this curve-fitting procedure is that all of these considerations are taken care of simultaneously and automatically, and the process is repeatable and stable.

In Fig. 7 noticeable oscillation of the data points about the prediction curve exists due to the kinematics of the manual positioning stages as they are adjusted between measurements. While these effects are worth mentioning because they appear consistently in the data sets, they do not heavily influence the results of the curve-fitting procedure.

From the process used to generate the results in Fig. 7, the calculated values of β_{11} are shown in Table 1 along with results from comparable works [26,27,25].

These results compare favorably to those found in literature, although it is important to note that the literature values in the cases of Yost and Cantrell [26] and Li et al. [27] are for specimens of aluminum that have undergone different heat treatments and are of different chemical compositions from those tested in Thiele et al. [25] and the current work. However, the fact that the current work falls within the ranges obtained by the other authors speaks

Table 1
Literature and current work data for nonlinearity parameter in comparable Al specimens.

Data source	Materials	$\beta_{11}^{7075}/\beta_{11}^{2024}$ (max–min)
Yost et al. [26]	Al 7075 Al 2024	1.865 (2.03–1.70)
Li et al. [27]	Al 7075-T551 Al 2024-T4	1.125 (1.28–0.97)
Thiele et al. [25]	Al 7075-T651 Al 2024-T351	1.675 (1.85–1.50)
Current work	Al 7075-T651 Al 2024-T351	1.363 (1.52–1.25)

to the accuracy of the proposed method for the calculation of the nonlinearity parameter.

Further results are obtained from a data set borrowed from Ruiz et al. [4] in which heat treatment of a duplex steel sample (2205 stainless) was performed and nonlinear ultrasonic measurements taken with a contact transducer and wedge (identical to the one shown in Fig. 1(b)) as a receiver. This method of measuring the nonlinearity parameter is inherently less precise than methods using air-coupled transducers because of the additional interfaces between the receiving wedge to the specimen and the receiving transducer to the receiving wedge. In cases like these where the variation of the data is large, guessing which points define the "linear region" of the data is highly prone to subjectivity, and avoiding this step makes results more reliable and repeatable.

By looking at the results of Fig. 8(a), the difference in the fitting of the calculated ratios of A_2/A_1^2 at 24 h of heat treatment between the linear and nonlinear fitting methods is clearly shown both quantitatively and qualitatively. The process used to calculate the linear fit is difficult to automate or standardize because the metrics that are typically used to deduce goodness-of-fit, such as an R-squared value, can often be misleading. If the linear fit is conducted over the entire data region, then the R-squared value would, in this case, be higher than in all other data ranges. However, this fit clearly does not follow the qualitative trend of the data and will become much worse with longer propagation distances in addition to demonstrating poorer accuracy in shorter propagation ranges. A linear fit to the first n data points that collectively define the "linear region" will be much more accurate in short propagation ranges but will rapidly lose accuracy in the far field. This effect was discussed briefly in Section 1 and is primarily due to the smaller contributions of attenuation and diffraction with small propagation distances. Because standard goodness-of-fit metrics are hard to apply, the most easily conducted method of determining the "linear region" is therefor by inspection, which has obvious subjective disadvantages rooted in human error. The quantitative disadvantages, however, become glaringly obvious in Fig. 8(a) at the propagation distance of 100 mm, where the linear fit no longer passes through the error bars of the measured data.

The question of repeatability, consistency, and accurate accounting of acoustic considerations in the far field versus short range accuracy before attenuation and diffraction begin to dominate is answered by the nonlinear fitting method in this work, the results of which are shown as the black dash–dotted line in Fig. 8(a). The nonlinear fit clearly shows strong accuracy to the measured data points as well as the ability to accurately reflect the trend of the data as it enters the far field. At all points in the measurement region, the nonlinear fit passes through the error bars of the data. These advantages are present in all of the measurements conducted on every specimen in the 2205 duplex stainless steel data set, and because the subjectivity of the linear fitting method is removed, the results are repeatable as well.

The calculated β_{11} values from both the linear (Ruiz data) and nonlinear (current work) methods are shown in Fig. 8(b). The agreement of the general trends between the data sets confirms that the nonlinear fitting method of extracting the nonlinearity parameter produces results that are comparable to those found in the earlier work. Additionally, one source of confusion with the results obtained from the linear fitting technique was the rise of the nonlinear parameter value at 24 h, labeled (**) in Fig. 8(b), back to the heat treatment levels obtained at 10 min, labeled (*) in Fig. 8(b), of treatment time. This trend was not observed in other material tests [28–30], and the nonlinear fitting method proposed in the current work shows results more in line with those expected from experience and literature [28]. The accuracy and repeatability of the nonlinear fitting approach combined with the more realistic

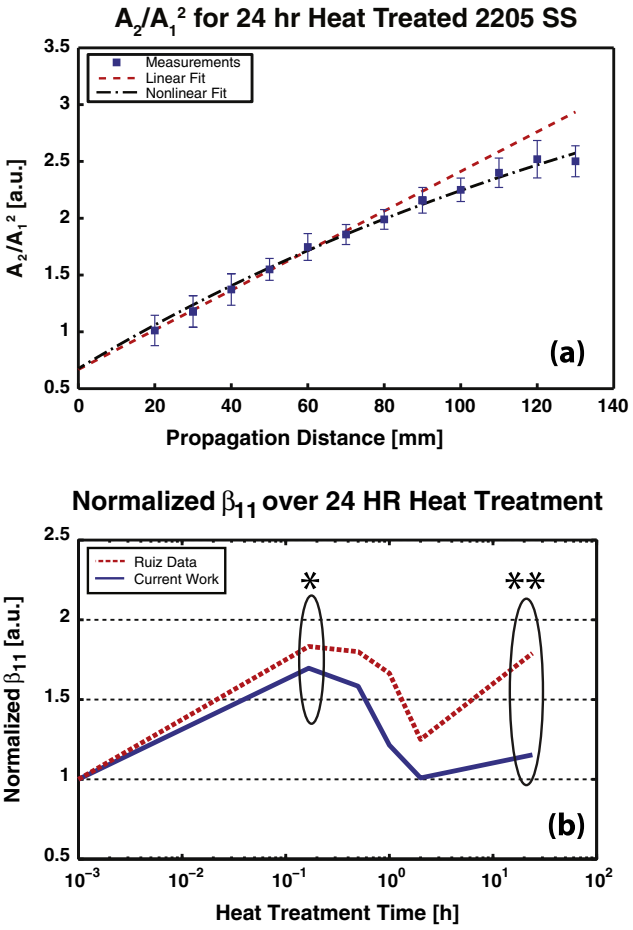

Fig. 8. (a) Shows a set of nonlinear measurements versus propagation distance for a 2205 SS sample heat treated over 24 h. The red dotted line shows a linear fit to the "linear region" of the data, which is identified subjectively. The black dash–dotted line represents the results of the nonlinear fitting procedure. (b) Shows the results of 2205 duplex stainless steel nonlinear parameter measurements as a function of heat treatment time for both the original analysis using a linear fitting approach (Ruiz et al.) and the nonlinear fitting approach (current work). The data point labeled (*) represents data collected at 10 min, and the data point labeled (**) represents data collected at 24 h. The β_{11} values represented by each fitting procedure in (a) can clearly be seen as the last data point in (b). (For interpretation of the references to colour in this figure legend, the reader is referred to the web version of this article.)

measures of β_{11} show the strengths of this procedure for calculating material nonlinearity.

5. Conclusions and future work

In this work, it is postulated that, given a Gaussian line source approximation for the generation of a Rayleigh wave, physically accurate values for a relative measure of the nonlinearity parameter can be extracted by fitting the data to models accounting for diffraction, attenuation and transducer nonlinearity effects. By showing that the source function, which is a result of the wedge and transducer combination, can be accurately described as Gaussian in shape, we validate the use of this approach. Furthermore, the experiments show that there exists a second harmonic component to the source function prior to generation effects from the sample material that is also Gaussian in shape, and that this effect must be accounted for in the model and the data. In order to fit the data taken from the air-coupled transducer setup to the proposed model, the use of a nonlinear least squares curve-fitting procedure is necessary because many of the parameters required for the fit process are either difficult to measure or directly immeasurable.

This process is done over multiple steps, the first fitting the fundamental frequency data, the second estimating the nonlinear source strength, and the third fitting the second harmonic attenuation and the nonlinear parameter, which is the ultimate desired result. This process is shown for Al 2024 and 7075 samples, and the results are consistent with previous literature and physical expectations. Additionally, a borrowed data set for heat-treated 2205 duplex stainless steel is re-processed with the updated analytical model and it is found that the new values for the nonlinear parameter both match with the general trends from the previous results and amend them to agree with past literature and physical expectations of the treatment process.

While this work details a more refined process for calculating the nonlinearity parameter from experimental results, more experimental information could facilitate more accurate estimations of the fitting parameters. Measurement of the attenuation at the fundamental and second harmonics could serve to either confirm or directly substitute these values in the model, meaning fewer parameters to fit and thus more accuracy from the model. In addition, directly measuring the source strengths with the laser vibrometer before each data collection would allow for substitution of that information into the analytical formulation, leaving just the nonlinear parameter as the sole fitting variable.

Another factor that is unknown in the procedure implemented in this work is the phase relationship between the fundamental and harmonic components of the source. This work treats these components as having the same phase, however phase differential could slightly alter the value of β_{11} calculated from the curve fitting procedure. While the reasonableness of the results in this paper validate the assumption about the relative phase, an experimental setup that could accurately and consistently calculate this quantity would answer this question definitively.

Additionally, the relationship of the output voltage from the air-coupled receiver to the received waveforms is more complicated than using an axial solution to the fitting equation because the transducer receives a signal from an area distribution about the central measurement axis. This spatial weighting is a transducer property and will be necessary to understand moving forward. In theory, if the receiving transducer is accurately characterized and the transfer function known exactly, then the results of this procedure would be absolute measures of the nonlinear parameter, which would be a very powerful tool in Rayleigh wave measurements for the NDE community.

Acknowledgements

We would like to acknowledge the U.S. Department of Energy Nuclear Energy University Program (NEUP) for funding this work. We would also like to thank Dr. Jennifer Michaels and her lab for the use of their Polytec LDV and positioning system for our laser measurements.

Appendix A. Derivation of diffraction equations

The following is a more detailed derivation of Eqs. (7) and (8) according to the steps listed primarily in Shull et al. [19]. First, we start with the quasilinear system given by Eqs. (3) and (4):

$$\left(\frac{\partial}{\partial x}+\frac{1}{2ik_0}\frac{\partial^2}{\partial y^2}+\alpha_1\right)v_1=0 \tag{A.1}$$

$$\left(\frac{\partial}{\partial x}+\frac{1}{4ik_0}\frac{\partial^2}{\partial y^2}+\alpha_2\right)v_2=-\frac{\beta_{11}k_0}{2c_R}v_1^2 \tag{A.2}$$

It is illustrative to note that these equations do not require the traveling wave to be plane. The lack of this condition stems from the derivation of the spectral equations from which the equations of motion (A.1) and (A.2) are formulated [17]. Now consider a source with the following conditions at $x=0$:

$$v_1(0,y)=w(y) \tag{A.3}$$

$$v_n(0,y)=0, n>1 \tag{A.4}$$

This source need not be symmetric, and may be complex.

The integral solutions to Eqs. (A.1) and (A.2) are formulated by employing a Green's function formulation, and are expressed in the following form:

$$v_1(x,y)=\int_{-\infty}^{\infty}w(y')g_1(x,y|0,y')\mathrm{d}y' \tag{A.5}$$

$$v_2(x,y)=-\frac{\beta_{11}k_0}{2c_R}\int_0^x\int_{-\infty}^{\infty}v_1^2(x',y')g_2(x,y|x',y')\mathrm{d}x'\mathrm{d}y' \tag{A.6}$$

where the Green's functions g_1 and g_2 are represented as:

$$g_1(x,y|x',y')=\sqrt{\frac{k_0}{i2\pi(x-x')}}\exp\left(-\alpha_1(x-x')+\frac{ik_0(y-y')^2}{2(x-x')}\right) \tag{A.7}$$

$$g_2(x,y|x',y')=\sqrt{\frac{2k_0}{i2\pi(x-x')}}\exp\left(-\alpha_2(x-x')+\frac{i2k_0(y-y')^2}{2(x-x')}\right) \tag{A.8}$$

Note that in the formulation of the Green's function for the velocity at the fundamental frequency (g_1) the propagation is considered from $(0,y')$, which is the location of the source. However, in the case of Green's function for the second harmonic velocity (g_2), the propagation is considered from all points on the surface (x',y'). This is due to the harmonic generation as the wave propagates and continually leaks energy from the fundamental frequency to its harmonics [17].

If we perform this integration and let $w(y)$ be defined as a Gaussian source function as in Eq. (6):

$$w(y)=v_0e^{-(y/a)^2} \tag{A.9}$$

then we have the necessary information to solve Eq. (A.5). To do this, we recast the integral into the form:

$$\int_{-\infty}^{\infty}e^{-ay'^2}e^{-2by'}\mathrm{d}y'=\sqrt{\frac{\pi}{a}}e^{(b^2/a)} \tag{A.10}$$

After simplification, we arrive at the solution for v_1 given in Eq. (7). To solve for v_2 in Eq. (A.6) is much more complicated, but uses the same general approach as in the solution for v_1 but with the added complication of the second integral in x'. An observation of solution given by Eq. (8) reveals two error functions. The first error function is associated with the particular solution and the second to the homogeneous solution to Eq. (4), where the particular solution describes the forced component and the homogeneous solution describes the free propagating component of the second harmonic wave [16].

References

[1] J. Herrmann, J.-Y. Kim, L.J. Jacobs, J. Qu, J.W. Littles, M.F. Savage, Assessment of material damage in a nickel-base superalloy using nonlinear Rayleigh surface waves, J. Appl. Phys. 99 (12) (2006) 124913–124914.
[2] S.V. Walker, J.-Y. Kim, J. Qu, L.J. Jacobs, Fatigue damage evaluation in A36 steel using nonlinear Rayleigh surface waves, NDT & E Int. 48 (0) (2012) 10–15.

[3] M. Liu, J.-Y. Kim, L. Jacobs, J. Qu, Experimental study of nonlinear Rayleigh wave propagation in shot-peened aluminum plates—feasibility of measuring residual stress, NDT & E Int. 44 (1) (2011) 67–74.
[4] A. Ruiz, N. Ortiz, A. Medina, J.-Y. Kim, L. Jacobs, Application of ultrasonic methods for early detection of thermal damage in 2205 duplex stainless steel, NDT & E Int. 54 (0) (2013) 19–26.
[5] J.S. Valluri, K. Balasubramaniam, R.V. Prakash, Creep damage characterization using non-linear ultrasonic techniques, Acta Mater. 58 (6) (2010) 2079–2090.
[6] S. Thiele, Air-coupled Detection of Rayleigh Surface Waves to Assess Material Nonlinearity due to Precipitation in Alloy Steel, Master's Thesis, Georgia Institute of Technology, December 2013.
[7] A.J. Croxford, P.D. Wilcox, B.W. Drinkwater, P.B. Nagy, The use of non-collinear mixing for nonlinear ultrasonic detection of plasticity and fatigue, J. Acoust. Soc. Am. 126 (5) (2009) EL117–122.
[8] M. Liu, G. Tang, L.J. Jacobs, J. Qu, Measuring acoustic nonlinearity parameter using collinear wave mixing, J. Appl. Phys. 112 (2) (2012) 024908.
[9] P.J. Westervelt, Parametric acoustic array, J. Acoust. Soc. Am. 35 (1963) 535.
[10] M.F. Hamilton, D.T. Blackstock, Nonlinear Acoustics, vol. 237, Academic Press, San Diego, 1998.
[11] M.B. Morlock, J.-Y. Kim, L.J. Jacobs, J. Qu, Mixing of two collinear Rayleigh waves in an isotropic nonlinear elastic half-space, 40th Annual Review of Progress in Quantitative Nondestructive Evaluation, vol. 1581, AIP Publishing, 2014, pp. 654–661.
[12] A. Ruiz, P.B. Nagy, Diffraction correction for precision surface acoustic wave velocity measurements, J. Acoust. Soc. Am. 112 (2002) 835.
[13] P.H. Rogers, A.L.V. Buren, An exact expression for the Lommel-diffraction correction integral, J. Acoust. Soc. Am. 55 (4) (1974) 724–728.
[14] G.S. Kino, Acoustic Waves: Devices, Imaging, and Analog Signal Processing, vol. 107, Prentice-Hall, Englewood Cliffs, NJ, 1987.
[15] F. Ingenito, A.O. Williams, Calculation of second-harmonic generation in a piston beam, J. Acoust. Soc. Am. 49 (1971) 319–328.
[16] D.J. Shull, E.E. Kim, M.F. Hamilton, E.A. Zabolotskaya, Diffraction effects in nonlinear Rayleigh wave beams, J. Acoust. Soc. Am. 97 (4) (1995) 2126–2137.
[17] E. Zabolotskaya, Nonlinear propagation of plane and circular Rayleigh waves in isotropic solids, J. Acoust. Soc. Am. 91 (1992) 2569.
[18] D.C. Hurley, Nonlinear propagation of narrow-band Rayleigh waves excited by a comb transducer, J. Acoust. Soc. Am. 106 (1999) 1782.
[19] D.J. Shull, M.F. Hamilton, Y.A. Il'insky, E.A. Zabolotskaya, Harmonic generation in plane and cylindrical nonlinear Rayleigh waves, J. Acoust. Soc. Am. 94 (1) (1993) 418–427.
[20] R. Smith, R. Stern, R. Stephens, Third-order elastic moduli of polycrystalline metals from ultrasonic velocity measurements, J. Acoust. Soc. Am. 40 (1966) 1002.
[21] C. Ramadas, A. Hood, I. Khan, K. Balasubramaniam, Effect of misalignment of air-coupled probes on A_o lamb mode propagating in a metal plate, Ultrasonics 54 (5) (2014) 1401–1408.
[22] M. Deighton, A. Gillespie, R. Pike, R. Watkins, Mode conversion of Rayleigh and Lamb waves to compression waves at a metal–liquid interface, Ultrasonics 19 (6) (1981) 249–258.
[23] D. Ensminger, L.J. Bond, Ultrasonics: Fundamentals, Technologies, and Applications, CRC Press, 2011.
[24] L.E. Kinsler, A.R. Frey, A.B. Coppens, J.V. Sanders, Fundamentals of Acoustics, fourth ed., John Wiley & Sons, Hoboken, NJ, 1999.
[25] S. Thiele, J.-Y. Kim, J. Qu, L.J. Jacobs, Air-coupled detection of nonlinear Rayleigh surface waves to assess material nonlinearity, Ultrasonics 54 (6) (2014) 1470–1475.
[26] W.T. Yost, J.H. Cantrell, The effects of artificial aging of aluminum 2024 on its nonlinearity parameter, in: D.O. Thompson, D.E. Chimenti (Eds.), Review of Progress in Quantitative Nondestructive Evaluation, Springer, 1993, pp. 2067–2073.
[27] P. Li, W. Yost, J. Cantrell, K. Salama, Dependence of acoustic nonlinearity parameter on second phase precipitates of aluminum alloys, in: IEEE 1985 Ultrasonics Symposium, 1985, pp. 1113–1115.
[28] Y. Xiang, M. Deng, F.-Z. Xuan, C.-J. Liu, Experimental study of thermal degradation in ferritic Cr–Ni alloy steel plates using nonlinear Lamb waves, NDT & E Int. 44 (8) (2011) 768–774.
[29] A. Viswanath, B.P.C. Rao, S. Mahadevan, P. Parameswaran, T. Jayakumar, B. Raj, Nondestructive assessment of tensile properties of cold worked AISI type 304 stainless steel using nonlinear ultrasonic technique, J. Mater. Process. Technol. 211 (3) (2011) 538–544.
[30] D. Barnard, G. Dace, O. Buck, Acoustic harmonic generation due to thermal embrittlement of Inconel 718, J. Nondestruct. Eval. 16 (2) (1997) 67–75.